Welding in the World (2023) 67:1967–1983
https://doi.org/10.1007/s40194-023-01547-x

RESEARCH PAPER

Interface characteristics and properties of nickel-based alloy coatings on cast iron fabricated by plasma and cold metal transfer wire-arc deposition

Wei Meng[1,2] · Yunlong Lei[1,2] · Xing Wang[2] · Qunshuang Ma[1,2] · Xiaohui Yin[1,2] · Yongchang Hong[3]

Received: 2 March 2023 / Accepted: 30 May 2023 / Published online: 6 June 2023
© International Institute of Welding 2023

Abstract

Nickel-based alloy deposition on cast iron surfaces is beneficial to improve wear and corrosion resistance and increase service life. In this paper, Inconel 625 nickel-based alloy on gray cast iron was wire-arc deposited by cold metal transfer process (CMTP) and plasma arc welding process (PAWP). The forming characteristics, microstructure, and interface behaviors of CMT and PAW deposits are comparatively studied. The results show that dilution rate of PAW deposited layers is significantly larger than that of CMT, and the latter interface presents "diffusion-metallurgical" bonding. Microstructure of CMT deposited layer is γ-Ni dendrite with (Nb, Mo) carbides distributed at the grain boundaries, and that of PAW deposited layer is a γ-(Fe, Ni) dendrite with eutectic carbides with complex morphology. The lamellar graphite near the interface is completely dissolved, and the microstructure is mainly ledeburite. CMT-deposited specimens exhibited significant cold cracking due to the inhomogeneous distribution of brittle high-carbon martensite and lamellar graphite in the partial melting zone and heat affected zone. Microhardness of PAW deposited layer was greater than that of CMT deposits, and the shear fracture near the interface of PAW and CMT samples presented intergranular fracture.

Keywords Wire-arc deposition · Gray cast iron · Nickel-based alloy · Interface · Mechanical properties

1 Introduction

Cast iron is widely used in many industrial fields such as machine tools and automotive engine parts due to its excellent casting performance and low cost [1, 2]. In particular, gray cast iron has good damping ability, which can effectively reduce noise and vibration, and is commonly used in bases or racks of electromechanical equipment [3]. Nevertheless, gray cast iron is often replaced by other high-cost alloys due to its rather brittle behavior and poor corrosion resistance, which significantly limit the development and promotion of its practical applications. Surface cladding treatment of gray cast iron can improve the service performance of gray cast iron and help to expand its application areas [4–6].

There are a variety of techniques available for the surface coating and/or cladding of Inconel 625, including gas tungsten arc welding [7, 8], laser cladding [9, 10], cold metal transfer welding, and gas metal arc welding [11, 12]. Huang et al. [13] used the bypass coupling micro-plasma arc welding to form a layer of Inconel 625 on the plate of QT-400

Recommended for publication by Commission I - Additive Manufacturing, Surfacing, and Thermal Cutting

Highlights
- Inconel 625 alloy on the ductile iron surface by CMT and PAW was deposited.
- The microstructure and interfacial behavior were strongly influenced by the dilution rate.
- Cold cracks were observed in PMZ and HAZ of CMT deposited specimens.
- The interfacial bond strength of the deposited layers was tested.

✉ Yunlong Lei
leiyunlong2021@163.com

[1] Key Laboratory of Green Fabrication and Surface Technology of Advanced Metal Materials (Anhui University of Technology), Ministry of Education, Ma'anshan 243002, China

[2] School of Materials Science and Engineering, Anhui University of Technology, Ma'anshan 243032, China

[3] School of Intelligent Manufacturing Engineering, Ma'anshan University, Ma'anshan 243032, China

nodular cast iron. The fusion zone near the interface between the cladding layer and the plate of QT-400 nodular cast iron has the largest Vickers hardness of 630 HV. Arias-González et al. [14] generated a NiCrBSi coating over flat substrates of gray cast iron and nodular cast iron by fiber laser deposition. It was found that gray cast iron sample presented a higher dilution than cast iron sample and that the resulting Ni-based coating presented a significantly superior hardness to the cast iron. Fesharaki et al. [15] compared the microstructures of the Inconel 625 coatings formed by laser cladding and TIG (tungsten inert gas) cladding, respectively, and observed that the laser cladding led to the formation of finer microstructure in the coatings. It needs to be pointed out that the high cost and high requirements for workpiece assembly for laser cladding have limited its applications in industry. The poor weldability of cast iron associated with the high content of carbon makes it very difficult to use traditional arc welding techniques to clad Inconel 625 of high quality on gray cast iron in contrast to the arc-cladding of Inconel 625 on stainless steels. Thus, it is of practical importance to develop a "new" technique for the cladding of Inconel 625 of on HT-250 Gy cast iron.

Currently, shielded metal arc welding and tungsten inert gas-shielded welding are mainly applied to the cladding of cast iron [16, 17]. Note that cracks are produced near the interface and heat affected zone due to the formation of brittle phases with high heat input for traditional welding methods [18, 19]. Besides, microstructure of gray cast iron is dominated by lamellar graphite, and the sharp edges of its graphite cavity structure are prone to crack generation even under low mechanical stress level [20]. The low heat input arc for overlay welding can reduce the dilution rate and help to avoid cracking and premature failure. As compared to conventional arc welding, cold metal transition (CMT) welding and plasma arc welding (PAW) have been widely used in steel and non-ferrous metal welding due to their stable welding process and low heat input[21–25]. Thus, CMT and PAW wire-arc surfacing for cast iron has good prospects for application.

CMT welding is characterized by a combination of melt-drop transition and wire feeding, with reciprocal arc "extinction-ignition," resulting in low heat input and dilution. He et al. [26] used CMT and tungsten inert gas shielded welding (TIG) to deposit Inconel 625 alloy on X80 pipes and found that the Laves phase in the CMT cladding layer was lower than that of TIG. Moreover, the deposition of nickel-based alloys on 316L stainless steel using CMT was able to obtain defect-free and low dilution deposited layers [27]. Feng et al. [28] comparatively studied the forming characteristics of Inconel 625 alloy deposited using laser powder deposition and wire-arc deposition, and found that laser deposition resulted in deposited layers with finer microstructure and lower dilution rate, while the deposition efficiency was lower. Plasma arc surfacing has significant advantages in energy concentration, arc stability, and low heat input when applied to metal arc deposition. In general, plasma cladding is mainly done by powder deposition, and plasma wire-arc surface deposition has rarely been reported [29]. Shen et al. [30] prepared high entropy alloy coatings by the multiple-wire plasma-arc fusion (TW-PAC) method. The results of this study contribute to the preparation of thick HEA coatings overlarge areas at low cost and with high efficiency and provide new insights into Cr-Fe–Ni-Tix HEA coatings. Xie et al. [31] fabricated Fe-Co-Mo alloy coatings on 40Cr steel using plasma overlay welding. Consequently, the high energy density of plasma arc welding tends to produce an excessive fusion ratio and inhomogeneous composition. Thus, the control of the dilution rate in PAW deposition are the keys to ensuring high-quality arc deposited layers.

Nickel-based alloys have excellent wear resistance, corrosion resistance, and high temperature oxidation resistance, which are widely used for surface modification materials [32–34]. Yu et al. [35] prepared nickel-based alloy coatings on gray cast iron using induction heating, and the wear performance of the coatings was significantly better than that of the substrate. Jeshvaghani et al. [36] used the TIG welding process to deposit a nickel-based alloy coating on ductile iron, and the hardness and wear resistance of the layer were higher than that of the substrate. Additionally, nickel-based alloys cladding on the surface of carbon steel, high-strength steel, and stainless steel result in cladding layers with low dilution rates and good interfacial bonding, and the surface wear and corrosion resistance are significantly better than that of the base material. Given this, nickel-based alloys for metal surface modification materials have become increasingly popular in recent years [37, 38]. As such, nickel-based alloys have significant application prospects for overlay welding on cast iron surfaces.

In this paper, Inconel 625 nickel-based alloy was deposited on the surface of gray cast iron using CMT and PAW wire-arc welding methods. The forming characteristics and microstructure of CMT and PAW deposited layers were studied comparatively, and the interfacial and elemental diffusion behavior was analyzed. Microhardness and interfacial bond strength of the deposited layers were also investigated.

2 Experimental materials and methods

HT250 (C: 3.55 wt.%, Si: 1.58 wt.%, Mn: 0.76 wt.%, Fe: Bal.) was used as the base material with the dimensions of 100 mm × 100 mm × 10 mm. Figure 1 shows the metallographic morphology of gray cast iron, presenting white ferrite, massive black pearlite, and lamellar graphite in a reticular distribution. Rust and oil were removed from cast iron surface with a grinder and sandpaper before wire-arc

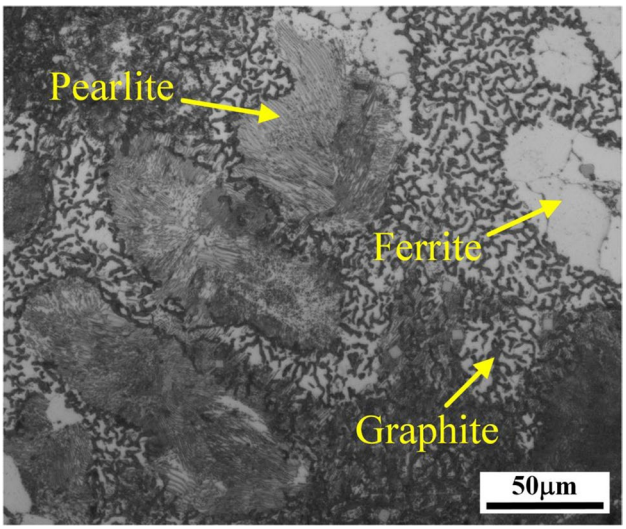

Fig. 1 Metallographic morphology of gray cast iron

deposition. The deposited material was ERNiCrMo-3 wire (Inconel 625) with a diameter of 1.2 mm (C: 0.01 wt.%, Si: 0.12 wt.%, Mn: 0.17 wt.%, Fe: 0.13 wt.%, Cr: 21.53 wt.%, Ni: 65.85 wt.%, Nb: 3.22 wt.%, Mo: 8.47 wt.%).

The CMT and plasma wire-arc deposition was selected to generate the coatings. The plates were mechanically ground and cleaned with acetone sequentially to remove surface debris and contaminants prior to the cladding of Inconel 625. A Fronius TPS 5000 CMT welding machine and a VR7000 wire feeder from Austria were used for wire-arc deposition. Plasma arc deposition on gray cast iron surfaces was performed using a Fronius TransTig 5000 Job G/F power supply and a Plasma Module 10 plasma generator. The wire feeder was a self-developed side-axis wire feeder with the model SB-10–500. High purity argon (99.999%) was used as the plasma gas and pure argon (99.99%) was used as the shielding gas for the deposition process. Single track and overlapped coatings were cooled in air. The relationship between wire-arc deposited parameters and geometrical characteristics and microstructure was investigated with gradual variation of a single processing parameter to explore the arc cladding processing map. The deposition process parameters for CMT and PAW are displayed in Table 1.

Metallographic specimens were cut from the cross-section of the deposited layer using a wire cutter and were ground and corroded. Because of the different corrosion characteristics of the deposited layer and gray cast iron, the deposited layer and gray cast iron were etched separately. The deposited layer was electrochemically etched with an $H_2C_2O_4$ aqueous solution at 6 V and 5 s. The gray cast iron was etched with 4% nitric acid alcohol. Microstructure was observed using a Zeiss AXIO optical microscope. The microstructure and elemental distribution were analyzed using a JSM-6510LV scanning

Table 1 Process parameters used for CMT and PAW deposition

Process parameters	Values	
	CMT	PAW
Current, A	95–170	120–200
Voltage, V	16.6–21.2	19.5–22.9
Wire feed speed, m/min	3.3–6.2	4
Welding speed, m/min	0.2	0.2
Heat inputs, J/mm	474–1081	702–1374
Shielding gas	Pure Ar	Pure Ar
Ar flow rate, L/min	20	20

electron microscope (SEM) and Oxford 6650 energy dispersive spectroscopy (EDS). The phase constitutions of the deposited layers were determined using a Bruker D8 advance X-ray diffractometer (XRD) with a scanning speed of 2°/min. The interfacial compression shear test was performed on a CMT-300 electronic universal testing machine at a rate of 1 mm/min. The dimensions of the compression shear die and specimen are depicted in Fig. 2. Microhardness was carried out on HV-1000 microhardness machine with a load of 4.9 N and a dwell time of 10 s at an interval of 0.3 mm.

3 Results and discussion

3.1 Forming characteristics

Figure 3 shows the surface morphology of CMT and PAW deposited layers under different heat inputs. As shown in Fig. 3, CMT deposited layer surfaces exhibit clear traces of melt pool change, and PAW deposited layer is smoother, which is due to the periodic fluctuation of melt pool with pulse cold metal transfer method, while DC power mode is employed for PAW deposition. In addition, severe cold cracks appear at the starting and closing arc positions. Moreover, the cracking tendency of CMT deposits is more significant with increasing heat input, and no cracks found in the PAW deposited layer when heat input is less than 1194 J/mm. The cracks mainly appeared on the substrate near interface rather than the deposited layer concerning lamellar graphite near the interface [39]. Note that the thermal input of PAW was greater than that of CMT, and no significant cracking was found in PAW deposition, which may be related to the difference in brittle phases near the interface. When heat input reached 1374 J/mm, transverse cracks that followed through the deposited layer appeared in the middle of PAW deposited layer. As a result, the heat input is not the main influencing factor causing the deposition cracks in gray cast iron, which is closely related to the brittle phase and flaky graphite near the interface.

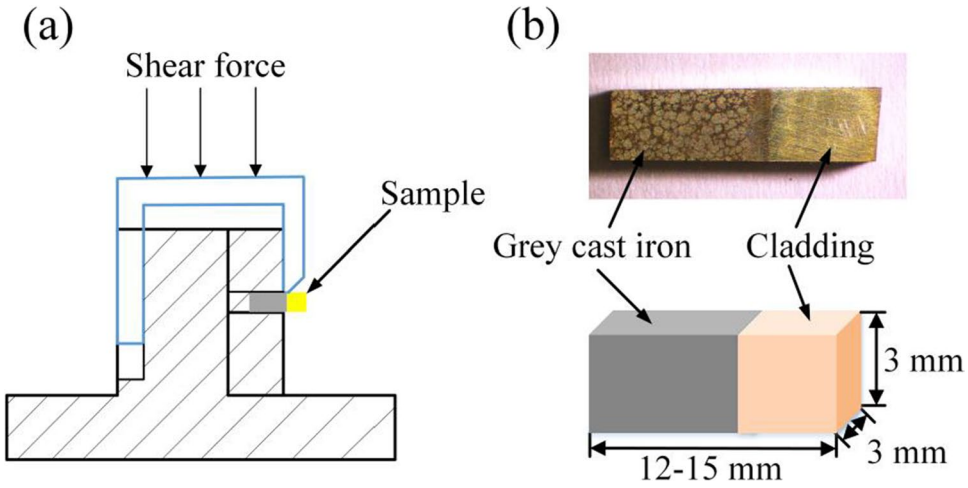

Fig. 2 Schematic diagram of the deposited specimen compression shear test and specimen size, **a** clamp, **b** specimen size

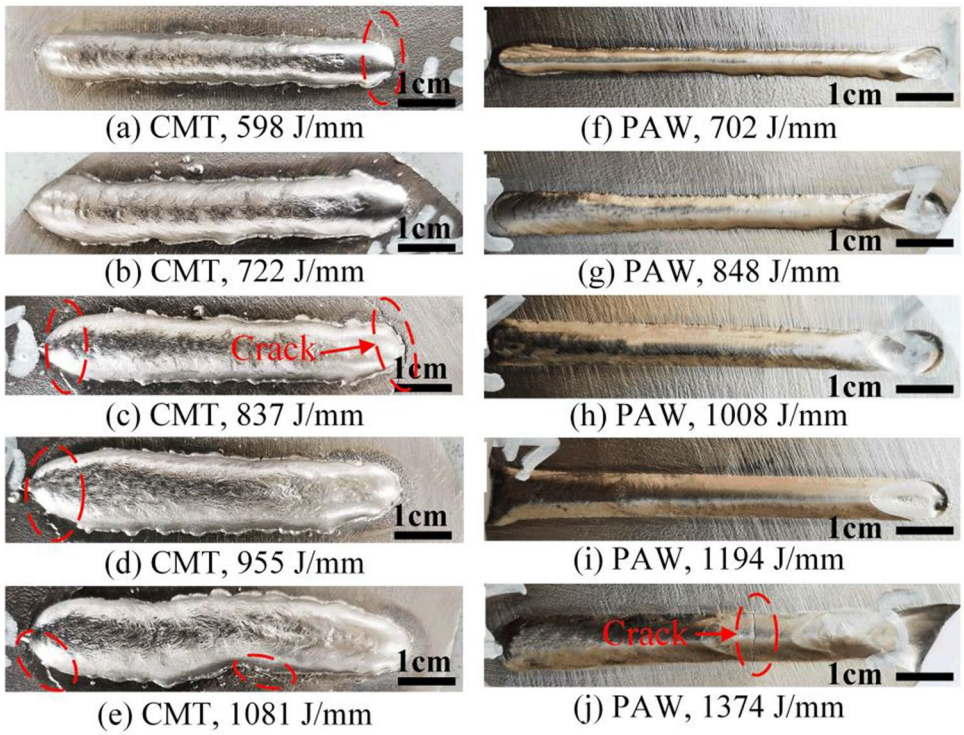

Fig. 3 Surface morphology of PAW and CMT deposited specimens, **a**–e CMT, **f**–**j** PAW

Figure 4 shows cross-sectional macroscopic morphology of CMT deposited layer under different heat inputs. As presented in Fig. 4, no defects such as cracks and porosity were found in the cross-section of CMT deposits, so cracks did not extend along the deposit direction. When heat input is lower than 598 J/mm, the deposited layer shows diffusion joining with the substrate, and the deposited profile displays a semi-elliptical morphology. When heat input reaches 1081 J/mm, the substrate on both sides of the deposited layer is also melted and the deposited layer achieves a complete metallurgical bond with the substrate. As the heat input increase, the impact of the arc on the melt pool is enhanced and the melt pool can exist longer, which is beneficial to the melting of the substrate on both sides [40, 41]. Figure 5 shows cross-sectional morphology of PAW deposited layers at different heat inputs. As shown in Fig. 5, the cross-sectional morphology of PAW deposited layer differs significantly from that of the CMT, presenting more base metal melting and a fan-shaped cross-sectional profile. With increased heat input, PAW interface is a typical metallurgical bond with the substrate considering the full melting of base metal. Regarding more plasma arc energy acting on the substrate and more substantial penetration, which results in a greater fusion region.

As seen in Fig. 6, the weld width and depth of CMT and PAW deposited layers increase with increasing heat input, and the height of both deposited layers has little variation.

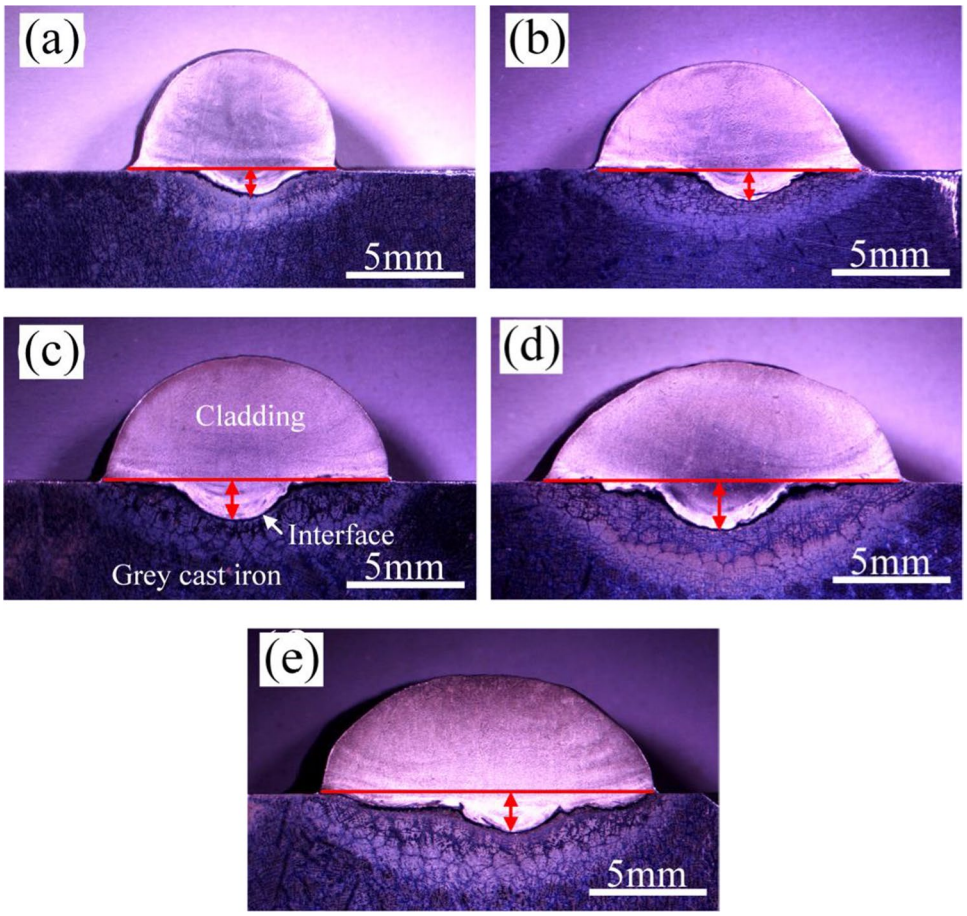

Fig. 4 Cross-sectional macroscopic profiles of CMT deposited layers with different heat inputs, **a** 598 J/mm, **b** 722 J/mm, **c** 837 J/mm, **d** 955 J/mm, **e** 1081 J/mm

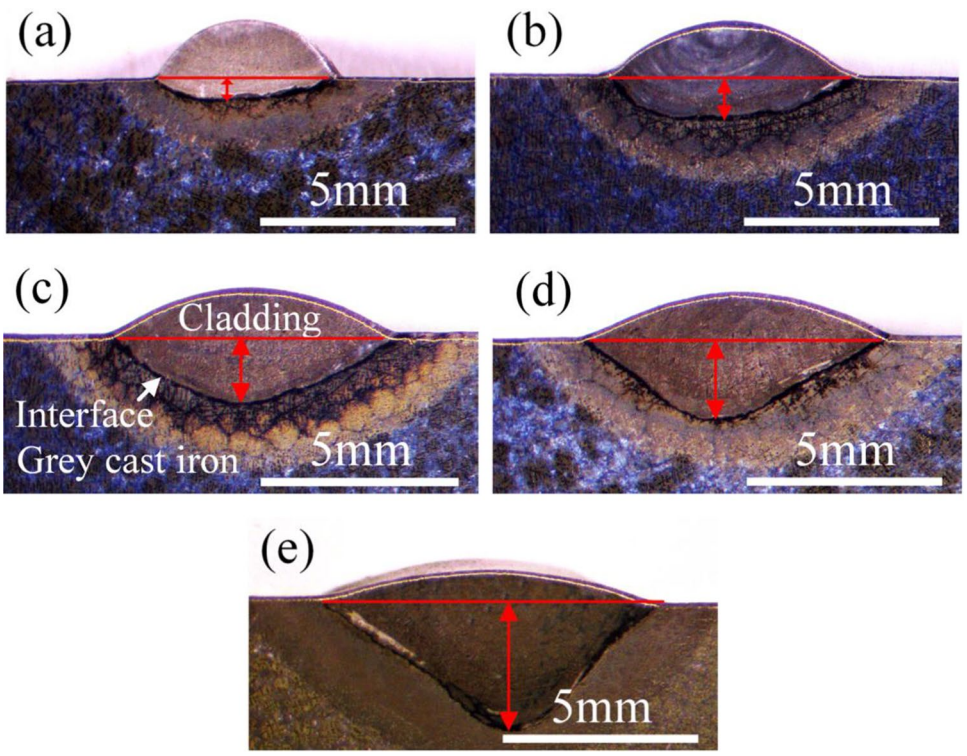

Fig. 5 Macroscopic morphology of PAW deposited layer cross-section at different heat inputs, **a** 702 J/mm, **b** 848 J/mm, **c** 1008 J/mm, **d** 1194 J/mm, **e** 1374 J/mm

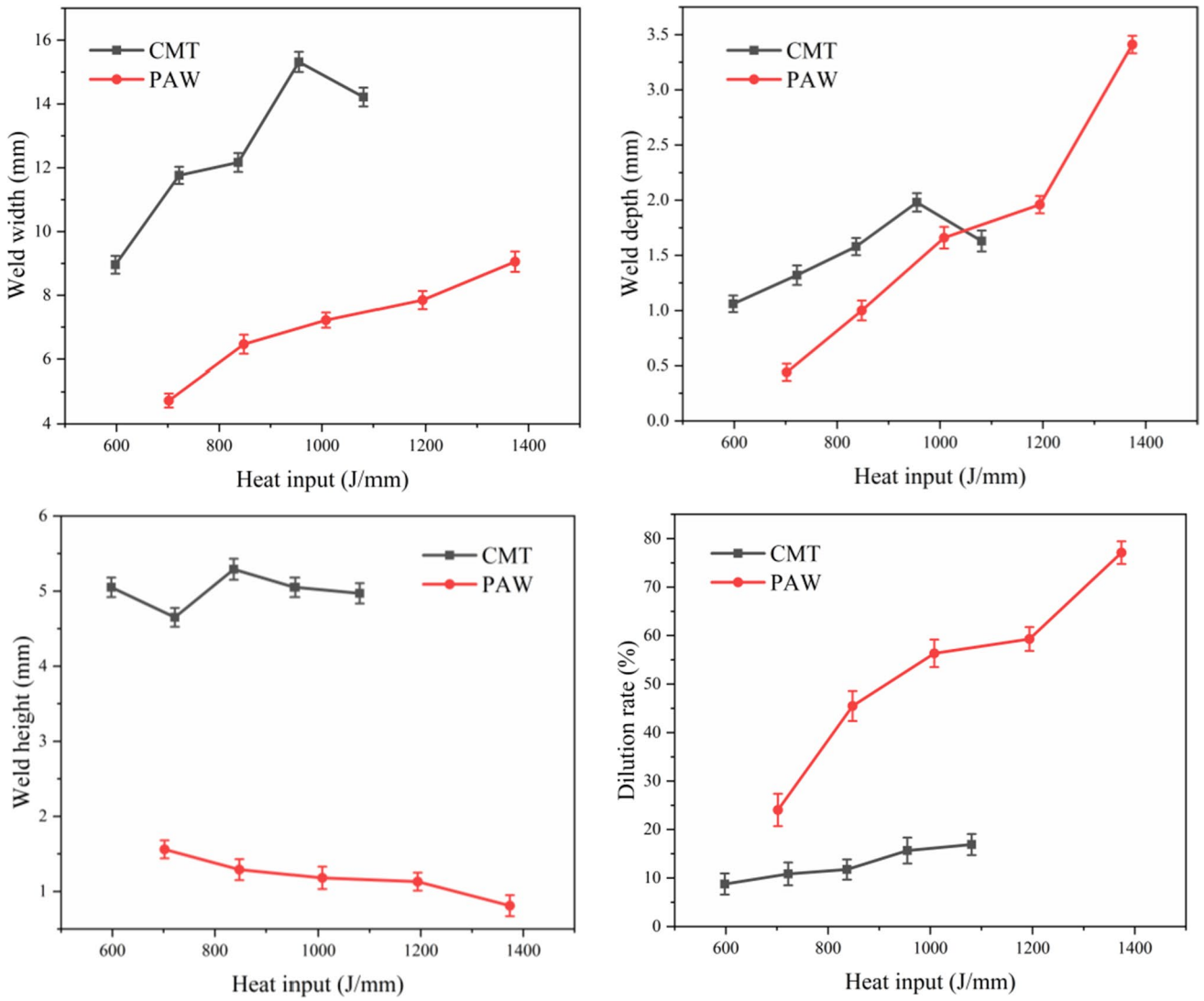

Fig. 6 Dimensions of the deposited layer under different processes and different heat inputs

Moreover, the height of PAW deposited layer is significantly lower than that of CMT, and the dilution rate of PAW deposits is larger. In the deposition, more base metal is melted into the deposited layer, which inevitably leads to significant changes in the composition distribution and microstructure of the deposited layer. Based upon forming dimensional measurements, the minimum dilution rate of PAW deposited layer is 24.03% and the maximum is 77.10%, while the maximum dilution rate of CMT deposited layer is 16.91%. Although a large dilution can ensure the metallurgical bonding of interface, inhomogeneous composition and brittle phases are more likely to be generated at large dilution rates.

In conclusion, no defects such as porosity and cracks are found in the deposited layer with 955 J/m thermal input of CMT deposition, and the spreading is good, which is favorable for cladding nickel-based alloys on cast iron surfaces. Furthermore, when the PAW heat input is less than 848 J/m, the deposited layer is well formed and the dilution rate is less than 50%, which is favorable to maintain the nickel-based alloy composition of the deposited layer and reduce the risk of cold cracks appearing.

3.2 Microstructure

Figure 7 shows the typical macroscopic and microstructure morphology of cross-sections of CMT and PAW deposited layer. As illustrated in Fig. 7a and b, the dilution rate and interface profile of CMT and PAW deposited layers show significant differences. A clear transition zone (white band region) appears near fusion line on two sides of the deposited layer, and the white zone in the middle of the interface is not obvious. Besides, a transition zone with a width of

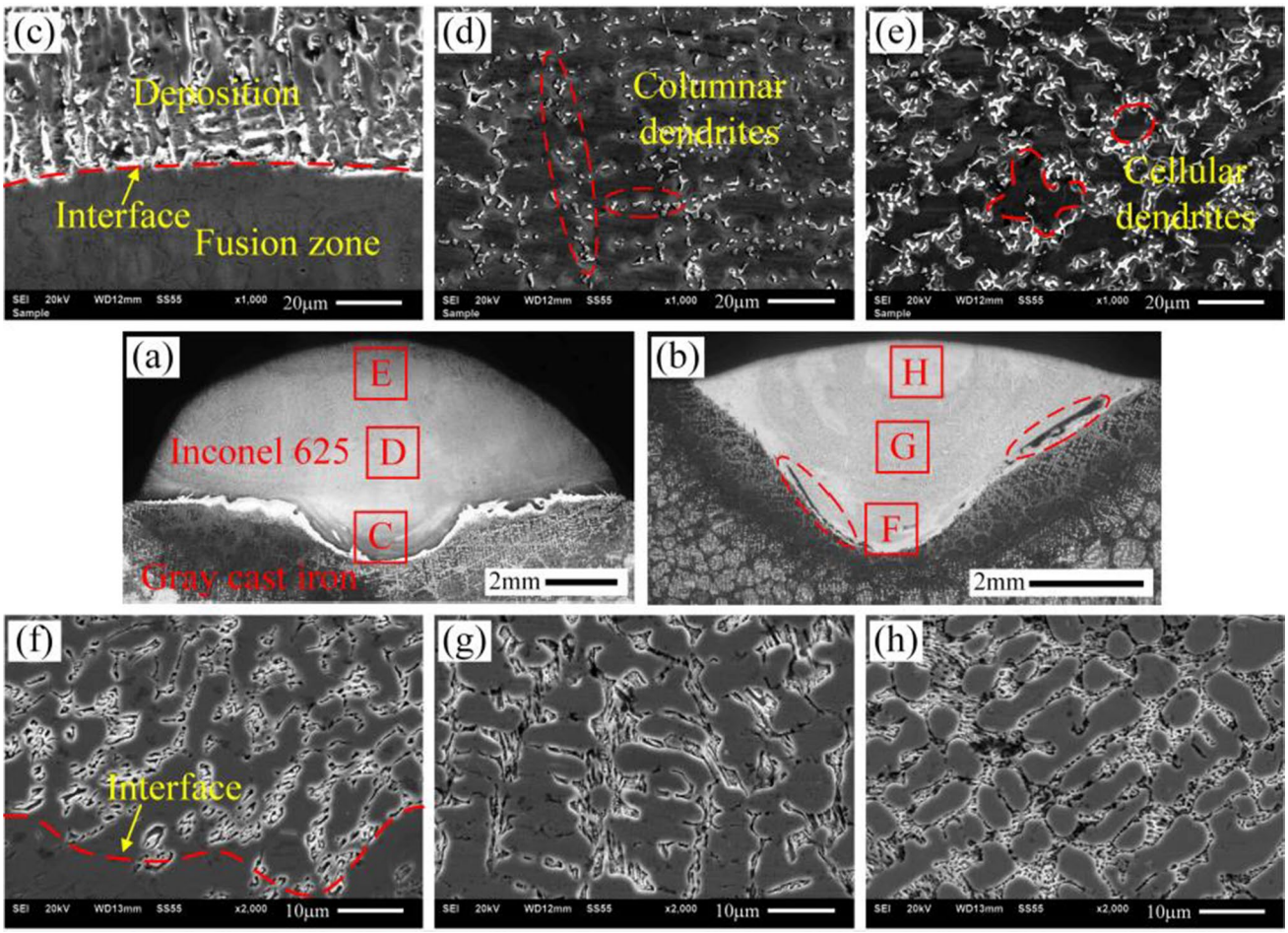

Fig. 7 Microstructure of different regions of CMT and PAW deposited specimens, **a**, **c**, **d**, **e** CMT, 955 J/mm, **b**, **f**, **g**, **h** PAW, 1374 J/mm, **c** magnification of C region, **d** magnification of D region, **e** magnification of E region, **f** magnification of F region, **g** magnification of G region, **h** magnification of H region

about 20 μm is found near the interface, and the graphite in this region has been completely dissolved. The molten base metal was not sufficiently mixed with the upper deposited layer, which is attributed to the fast cooling rate and solidification before fusion into the deposited layer. Regarding large fusion ratio in PAW deposits, the melt pool stirred more vigorously, resulting in an inconspicuous transition zone, as displayed in Fig. 7b.

Figure 7c–e shows microstructure near the interface of CMT deposited layer. As seen in Fig. 7c, the interface of CMT deposited layer presents epitaxial solidification, which is dependent on the upward growth of the grains in the partially melted zone (PMZ). The bottom of the deposited layer is columnar grain morphology, with more segregative phases appearing at the grain boundaries. The middle part of the deposited layer is mainly columnar dendrites, the precipitated phase shows a reticulated distribution, and the top part is cellular dendrites and largely precipitated phases at the grain boundary. Figure 7f–h shows microstructure near the interface of the PAW deposited layer. No precipitated phases are found at the grain boundary of PAW deposited layer, showing a high-temperature ferrite morphology. The crystalline morphology evolves from the bottom to the top as columnar to dendritic crystals and then cellular crystal. Consequently, the main composition of the deposited layer changes from Ni–Cr, a nickel-based alloy, to Fe–Ni-Cr, a mixed composition with the base metal. Furthermore, a large amount of dissolution of lamellar graphite leads to higher carbon content in the deposited layer.

In the deposition of nickel-based alloys, the composition of the crystallization front is much larger in terms of supercooling, and Cr, Mo, and Nb elements are more likely to segregate, and (Cr, Mo, Nb) carbides appear at the grain boundaries. Moreover, more melting base metal interfuses the deposited layer with larger dilution rate for PAW, resulting in non-uniform distribution of composition under rapid solidification conditions. As such, the composition of the deposited layer is altered, and the aggregation process near

the grain boundaries also changes significantly. Similarly, the crystallization process of PAW and CMT is different due to the variations of solute elements and compositional supercooling, which inevitably leads to different crystalline morphology. Hence, the grain morphology between the bottom and the top of the deposited layer is determined by the change in temperature gradient and compositional supercooling.

A black strip appears near the interface of the PAW deposited layer as shown in Fig. 7b. An EDS surface scan of this region was performed under the illumination of Fig. 8. The main elements in the black strip region are Ni, Cr, Nb, and Mo, which is consistent with the composition of nickel-based alloy due to the cooling near the interface and insufficient mixing of nickel-based alloys and cast iron.

To further determine the phase composition in the deposited layers, an energy spectrum analysis of the deposited layers was performed. Figure 9a shows the EDS point scan of CMT deposited layer. As demonstrated in Fig. 9a, the composition of CMT deposited layer is close to the Inconel 625 alloy composition, mainly Ni, Cr, and Mo. The dendrites are mainly γ-Ni solid solution, and the Fe content is slightly lower than that of the Inconel 625 alloy due to little cast iron fusing into the deposited layer. It is noted that Nb and Mo elements are significantly more abundant at the grain boundaries than that of dendrite interior, so that the precipitated phases along the grain boundaries are mainly (Nb, Mo) carbides. In general, the segregation of Nb and Mo elements at the grain boundaries during cooling due to the low solubility of Nb and Mo elements in the γ-phase and the dissolution and diffusion of lamellar graphite in the deposited layers generated a large number of carbide phases to be produced at the grain boundaries [42]. Figure 8b illuminates the point scans of different regions of the PAW deposited layers. As presented in Fig. 9b, the main composition of PAW deposited layer differs significantly from that of Inconel 625 alloy, with Fe element content exceeding 60%, which is much larger than the Ni element content. As a result, the transformation of the deposited layer is from Ni-based alloy to Fe-based alloy with the melting of excessive base metal. The composition difference between the grain boundary and intracrystalline is not significant, and no obvious elemental segregation is found. Moreover, the grain boundary is mainly a high-temperature ferrite dominated by (Fe, Ni) solid solution and a eutectic organization composed of (Fe, Ni, Cr) solid solution and carbide. Note that a granular precipitation phase formed in the grain, demonstrated as (Nb, Mo) carbide segregation phase in Fig. 9b.

Figure 10 and Fig. 11 show microstructures near the interface of CMT and PAW deposited layers. As shown in Fig. 10a, cross-sectional morphology of CMT deposited specimen is divided into five regions, which are deposited layer, fusion zone (FZ), partially melted zone (PMZ), heat-affected zone (HAZ), and substrate. The microstructure of fusion zone is illustrated in Fig. 10b. The lamellar graphite has been completely dissolved in FZ, and its microstructure is mainly γ-(Fe, Ni) and a large amount of carbide segregation at the grain boundary. Microstructure of PMZ is mainly composed of ledeburite (L), martensite (M), and not completely dissolved graphite (G), which presents unevenly distributed, and mainly dominated by brittle phases as depicted in Fig. 10c. Obviously, cracks can easily develop from FZ. Figure 10d shows microstructure of the upper heat-affected zone. The microstructure presents high-carbon twin martensite, along with incompletely dissolved graphite, and yet the lamellar structure of graphite has disappeared. The microstructure of lower heat affected zone is still pearlite (P) and lamellar graphite in Fig. 10f.

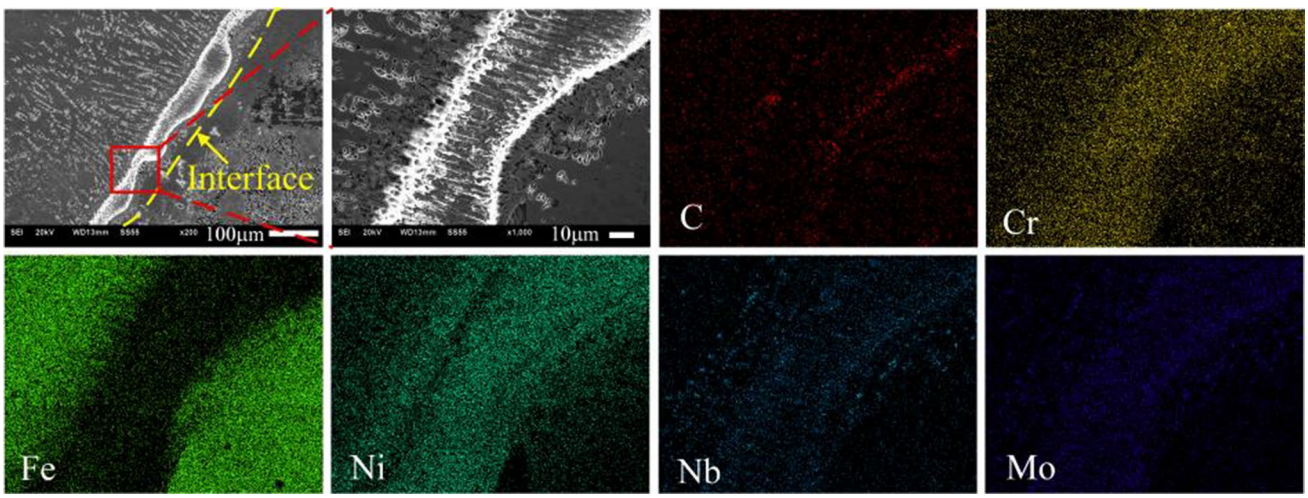

Fig. 8 EDS surface scan at the interface of PAW deposited layers

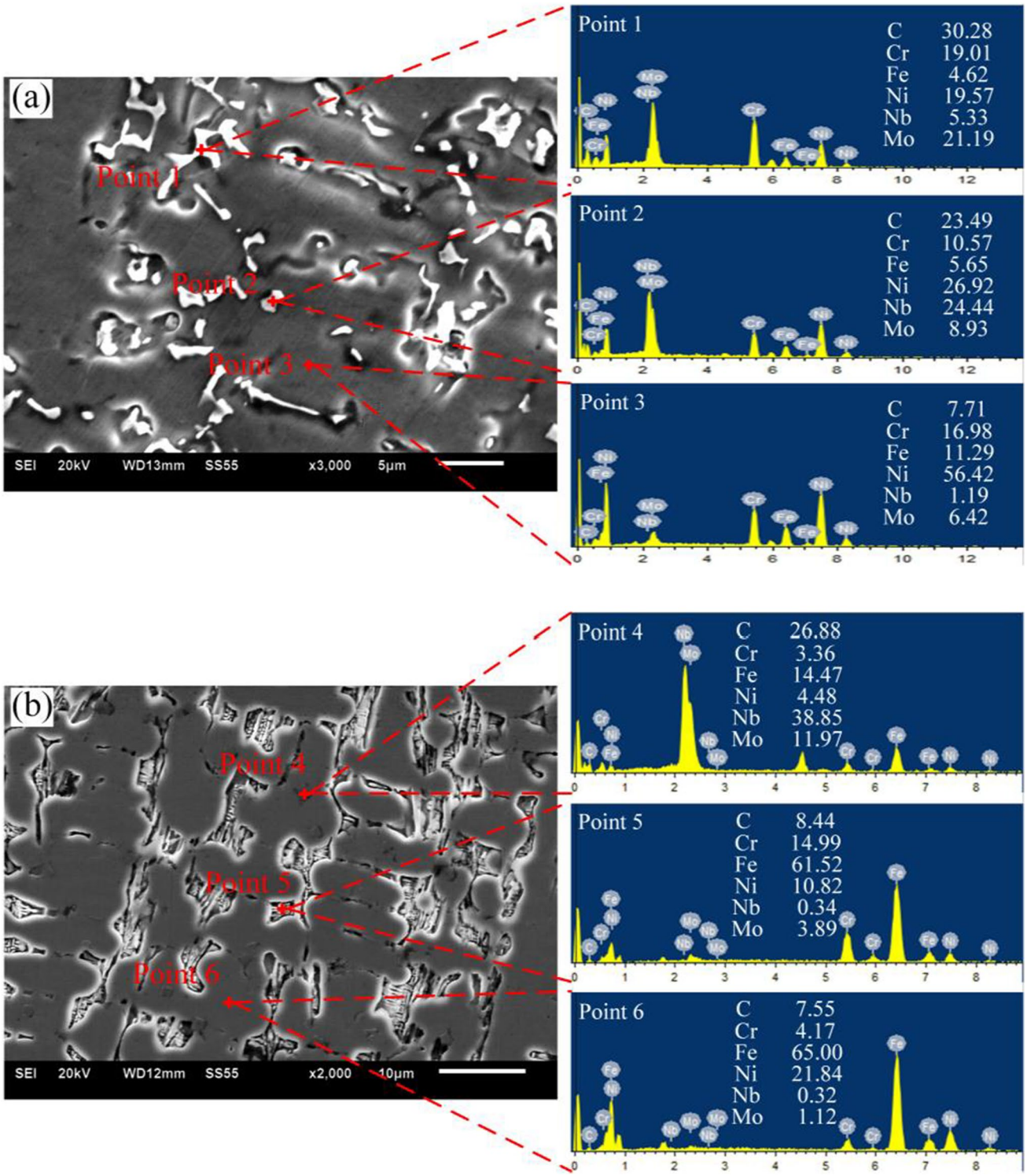

Fig. 9 EDS point scans of different locations of CMT and PAW deposited layers, **a** CMT 955 J/mm, **b** PAW, 1374 J/mm

Nevertheless, the macroscopic cracks appeared in both heat-affected zone and partially melted zone, with smaller cracks of 714.29 μm and larger cracks up to 1.7 mm in length. The cracks mainly extend along the lamellar graphite, as displayed in Fig. 10e and g. Furthermore, a large amount of brittle phases (high-carbon martensite and carbide) are generated in the PMZ and HAZ, which cuts the continuity between the base phases. Under certain thermal stress

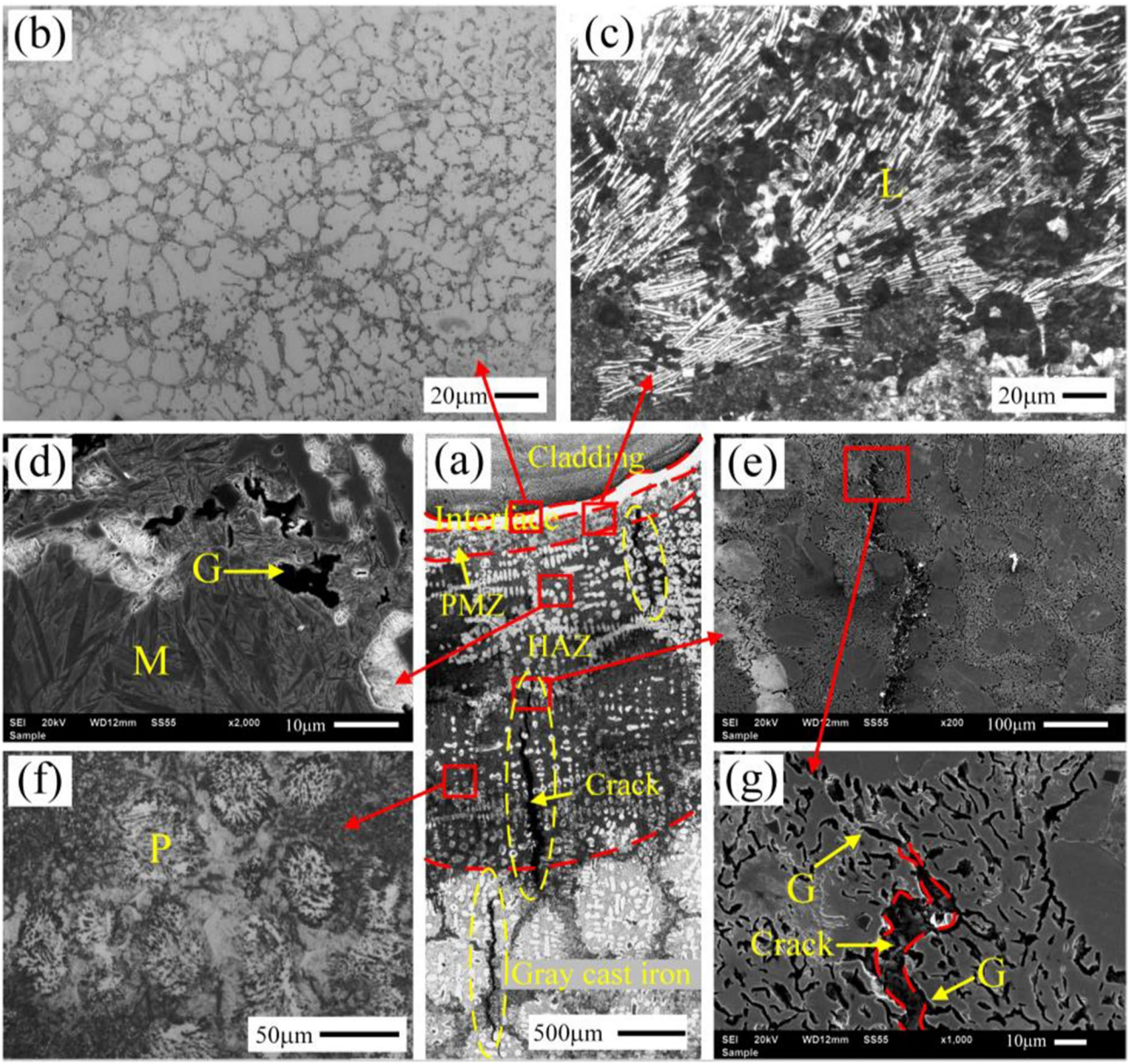

Fig. 10 Microstructure of the area near the interface of the 955 J/mm deposited specimen by CMT, **a** macroscopic micrographs, **b** microstructure of the interface region, **c** microstructure of the PMZ, **d** and **f** microstructure of the HAZ, **e** and **g** Magnification of crack region

conditions, the brittle phase and lamellar graphite are highly susceptible to crack generation [43].

Figure 11 shows microstructure near the interface of PAW deposited layer. As described in Fig. 11b, non-uniform composition distributes near the interface due to more melted base metal in PAW deposition. Figure 11c shows microstructure of partially melted zone of PAW deposits. The ledeburite and martensitic were produced in PMZ because of partial dissolution and diffusion of lamellar graphite. Microstructure of the upper heat-affected zone is mainly fine massive martensite, as presented in Fig. 11d. In PAW deposit, carbon diffuses into the austenite and transforms into martensite during the subsequent cooling [44]. As shown in Fig. 11e, graphite only appears to diffuse in the lower part of HAZ, which did not affect the morphology of graphite, and its microstructure was flaky graphite and pearlite, and a small amount of pristine ferrite.

Figure 12 shows EDS line scan from the deposited layer of Ni-based alloy to cast iron. Figure 12a illuminates EDS analysis of CMT deposited sample. Consequently, according to Fig. 12a, Ni, Cr, and Fe elements are more uniformly distributed in the deposited layer, and Nb and

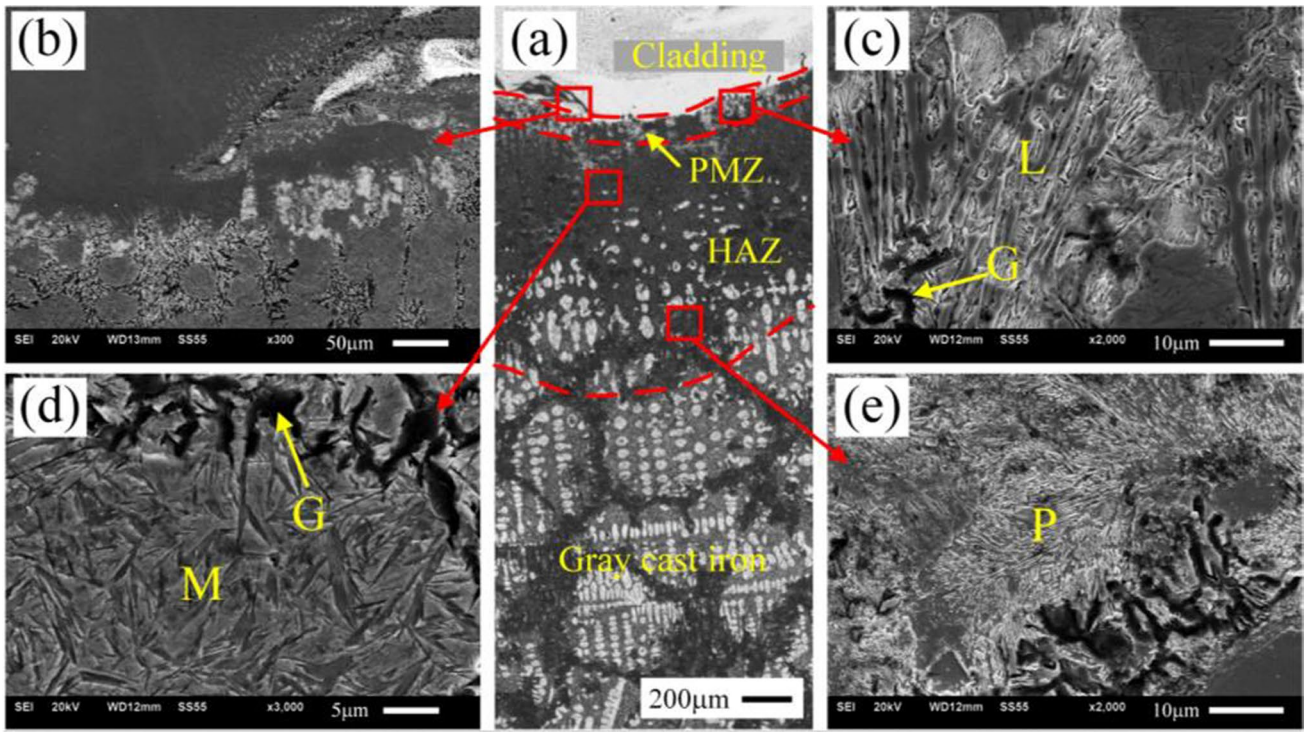

Fig. 11 Microstructure of the area near the interface of the 1374 J/mm deposited specimen by PAW, **a** macroscopic micrographs, **b** microstructure of the interface region, **c** microstructure of the PMZ, **d** and **e** microstructure of the HAZ

Mo elements show significant fluctuations owing to segregation at the grain boundaries. Moreover, no obvious composition transition zone was found at the interface, and a sudden change in composition from the deposited layer to the cast iron was observed. Particularly, significant fluctuations of carbon elements can be found in the cast iron region, which is mainly due to the presence of lamellar graphite, which is closely related to the morphology of graphite. Little fluctuation of carbon in the fusion zone is attributed to the sufficient dissolution of graphite. Figure 12b shows EDS analysis of PAW deposited sample. The element distribution of the deposited layer is significantly different from that of the CMT. Fe content decreases in a gradient from the interface to the deposited layer, which is attributed to differences in cooling rate and flow behavior of the melt pool. The elements such as Ni, Cr, Nb, and Mo show fluctuations due to the segregation of carbide or Laves phase in the crystal and grain boundaries. As described above, the base metal melted at the interface is fully mixed with the deposited layer, and the alloying elements at the PAW interface show abrupt changes with no gradient change, as depicted in Fig. 12b.

Figure 13 shows the XRD patterns of different regions of CMT and PAW deposited layers. As shown in Fig. 13, CMT deposited layer is mainly γ-Ni and the precipitated phase is mainly NbC, and PAW deposited layer is mainly γ-(Fe, Ni) and (Cr, Fe, Ni) eutectic. XRD peaks at the interface of CMT and PAW are mainly γ-(Fe, Ni), martensite and austenite, which is consistent with the previous microstructure analysis. XRD pattern did not reveal the presence of obvious carbides, which is mainly due to the low content of precipitated phases of Nb and Mo.

Figure 14 shows macroscopic morphology of CMT and PAW multi-pass deposited specimens. As shown in Fig. 14, surfaces of PAW and CMT deposited specimens are flat and good metallurgical bonding of interface was generated, and no defects such as pores and cracks are found. The melting depth of PAW deposited layer is significantly larger than that of CMT, which inevitably has more thermal influence on the substrate. In order to avoid cracking and to reduce the thermal impact on the substrate, it is appropriate to choose CMT deposition with a low dilution rate for gray cast iron.

Note that CMT and PAW deposits have low heat input arc characteristics, and the difference between the two deposition methods is mainly arc energy distribution and wire feeding type. Figure 15 shows schematic diagram of microstructure evolution at the interface between CMT and PAW deposited specimens. As displayed in Fig. 15a and c, CMT deposition layer is lower dilution rate and less cast iron is fused into the deposition layer, and a small amount of Ni and Cr elements diffuse out of the fusion zone. Compared with CMT, the dilution rate of PAW deposition layer is larger, and a

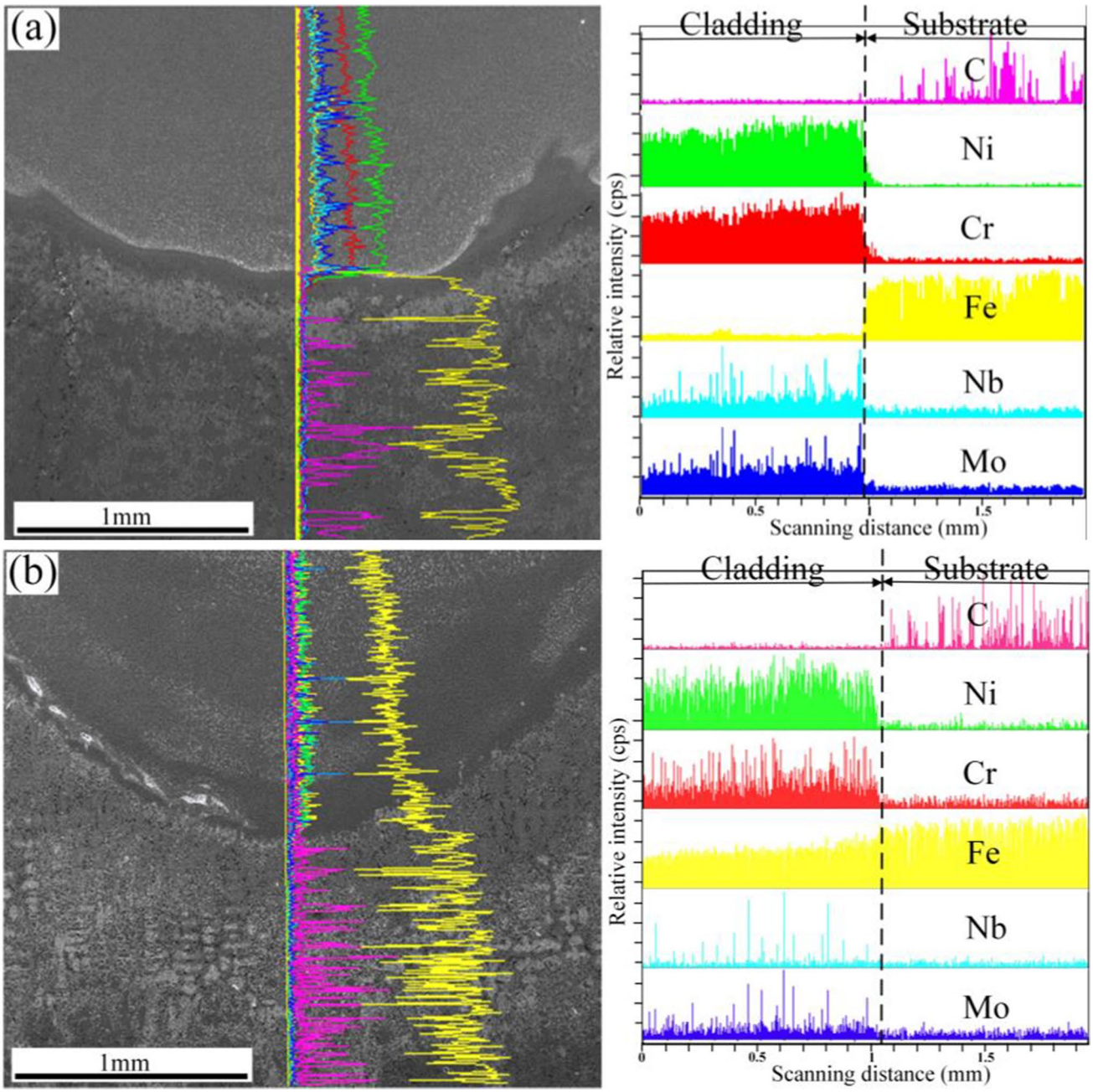

Fig. 12 EDS line scan near the interface of CMT and PAW deposited specimens, **a** CMT, 955 J/mm, **b** PAW, 1374 J/mm

large amount of Fe and C elements mix into the deposition layer through melt pool flow and thermal diffusion. As presented in Fig. 15b and d, the deposited layer of CMT shows mainly columnar grain, and that of PAW is dendritic due to the greater compositional supercooling. CMT deposited layer grain boundaries are mainly Nb and Mo segregative phases. In contrast, no obvious precipitated phases were found at the grain boundaries of PAW deposits. The width of partially melted zone of CMT deposited layer is larger and lamellar graphite is completely dissolved, finally forming ledeburite and martensite. Compared with PAW, martensite in the heat affected zone of CMT is coarser. It is noteworthy that the heat affected zone of CMT deposited specimens showed a significant tendency to cold cracking, with cracks extending from partially melted zone to heat affected zone, then expanding along lamellar graphite toward the matrix. Macroscopic cracking throughout the

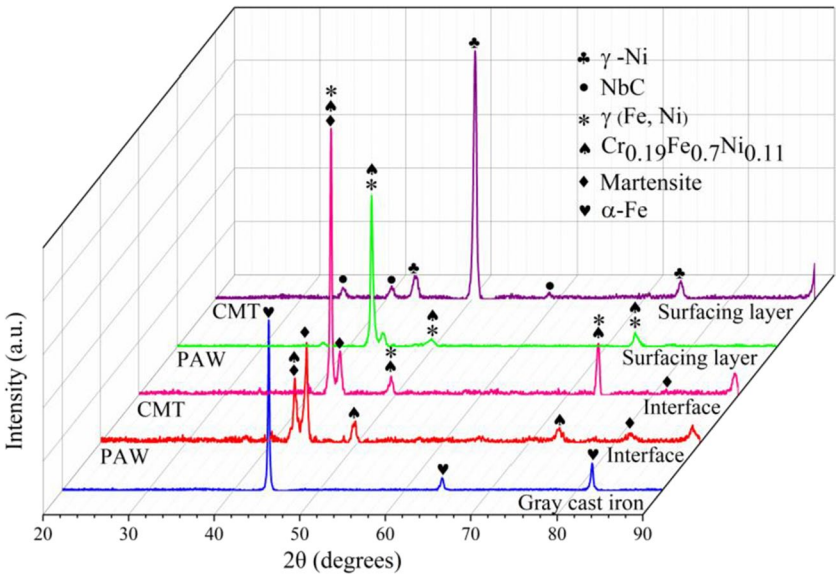

Fig. 13 XRD patterns of different regions of the CMT and PAW deposited samples

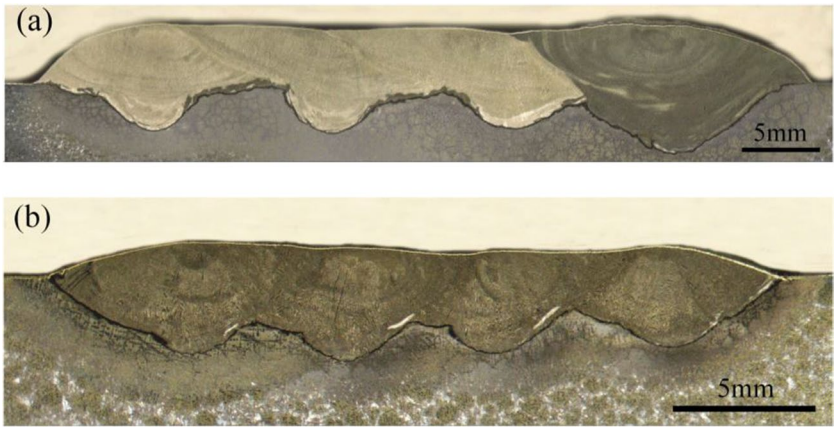

Fig. 14 Macroscopic morphology of CMT and PAW multi-pass deposited specimens, **a** CMT, 955 J/mm, **b** PAW, 1374 J/mm

specimen, which was mainly caused by the brittle phase such as ledeburite and martensite, formed in PMZ near the CMT interface and the incompletely dissolved lamellar graphite [10].

To sum up, the dilution rate of CMT deposited layer is lower than that of PAW, showing diffusion-metallurgical bonding, while the interface of PAW presents metallurgical bonding. CMT and PAW deposited samples no white mouth tendency was found in any of the deposited layers, but the flake graphite and high-carbon martensite in their heat-affected zones were prone to cold cracking. Microhardness of PAW deposited layer is greater than that of CMT, and that of both deposited layer is significantly higher than gray cast iron substrate, which is consistent with the experimental results of other cladding methods. Compared to laser cladding and conventional arc surfacing, CMT deposition presents a lower dilution rate for the same heat input, while its single layer deposition thickness (> 5 mm) is significantly higher than laser cladding (< 2 mm). Plasma arc deposition showed a higher dilution rate (> 50%) compared to less than 20% for general arc welding. As a result, CMT and plasma arc wire-arc deposition have lower heat input than conventional arc surfacing and significantly higher deposition efficiency than laser cladding.

3.3 Microhardness

Figure 16 shows microhardness distribution of CMT and PAW deposited specimens. As seen in Fig. 16, microhardness of the deposited layer is significantly higher than that of cast iron, and that of PAW deposited layer

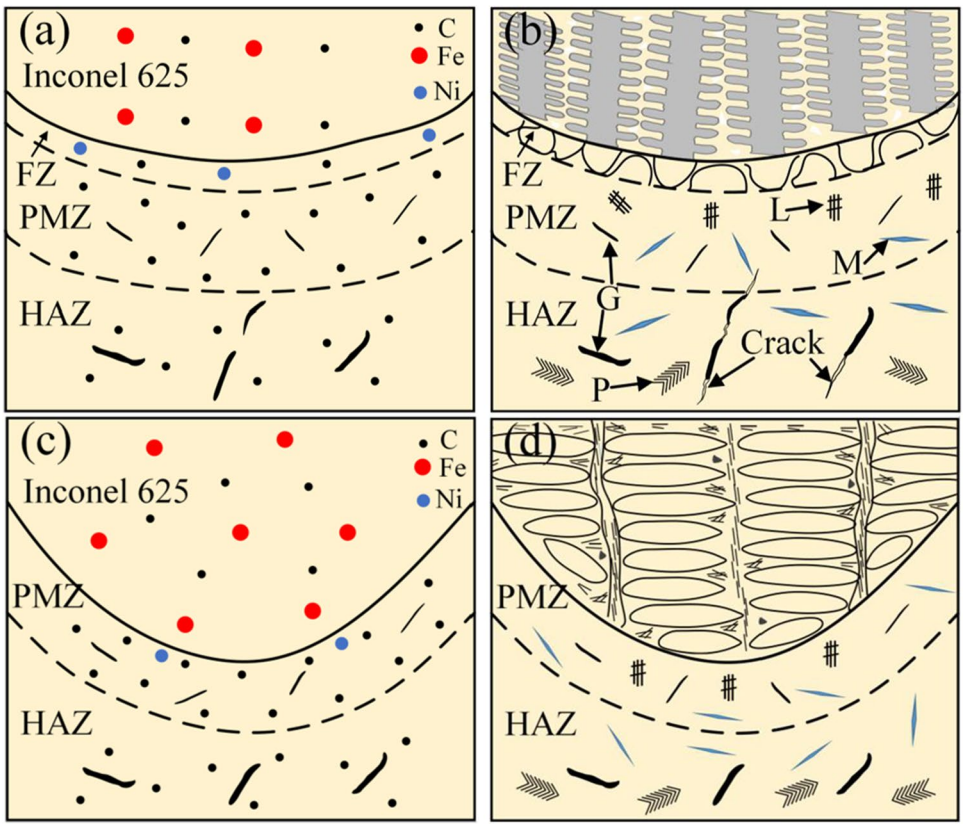

Fig. 15 Schematic diagram of the microstructure evolution at the interface between CMT and PAW deposited specimens, **a**, **b** CMT; **c**, **d** PAW

is significantly greater than that of CMT deposited layer, which is 438.54 $HV_{0.5}$ and 266.3 $HV_{0.5}$, respectively, while the average microhardness of grey cast iron is 185.7 $HV_{0.5}$. The massive melting of Fe and C elements in the PAW deposited layer plays a solid solution strengthening effect. The highest hardness occurs in PMZ near the heat affected zone, which is due to the partial dissolution of lamellar graphite near the interface, and the high carbon content forms a large amount of martensitic and ledeburite. The maximum hardness values exceed 600 $HV_{0.5}$.

3.4 Interfacial bond strength

Figure 17 presents the displacement-stress curve for deposited specimen shear test. The interfacial shear strengths of CMT and PAW deposited samples do not differ much, and both fracture in the heat-affected zone near the interface with an average strength of 406.67 MPa and 411.47 MPa, respectively. Figure 18 shows SEM morphology of the fractures of CMT and PAW deposited interfacial shear specimens. As shown in Fig. 18, the fractures of both show smooth step-like and lamellar shapes, with obvious intergranular fracture characteristics. Moreover, the microcracks and microscopic shrinkage holes distributed among lamellae. The weak interfacial bonding between lamellar graphite and ferrite and the graphite was dislodged or fractured to form microscopic shrinkage [45]. More microscopic shrinkage holes were generated at the PAW fracture surface than at the CMT, and probably the former has more graphite in the PMZ.

4 Conclusion

In summary, well-formed deposited specimens can be obtained without defects with the appropriate CMT and PAW deposition processes. Compared to laser cladding and conventional arc surfacing, CMT deposition presents a lower dilution rate for the same heat input. Plasma arc deposition showed a higher dilution rate compared to general arc welding; the main conclusions are the following:

1. Compared with PAW, the dilution rate of CMT deposited layer is lower than that of PAW, showing “diffusion-metallurgical” bonding, while the interface of PAW presents metallurgical bonding.

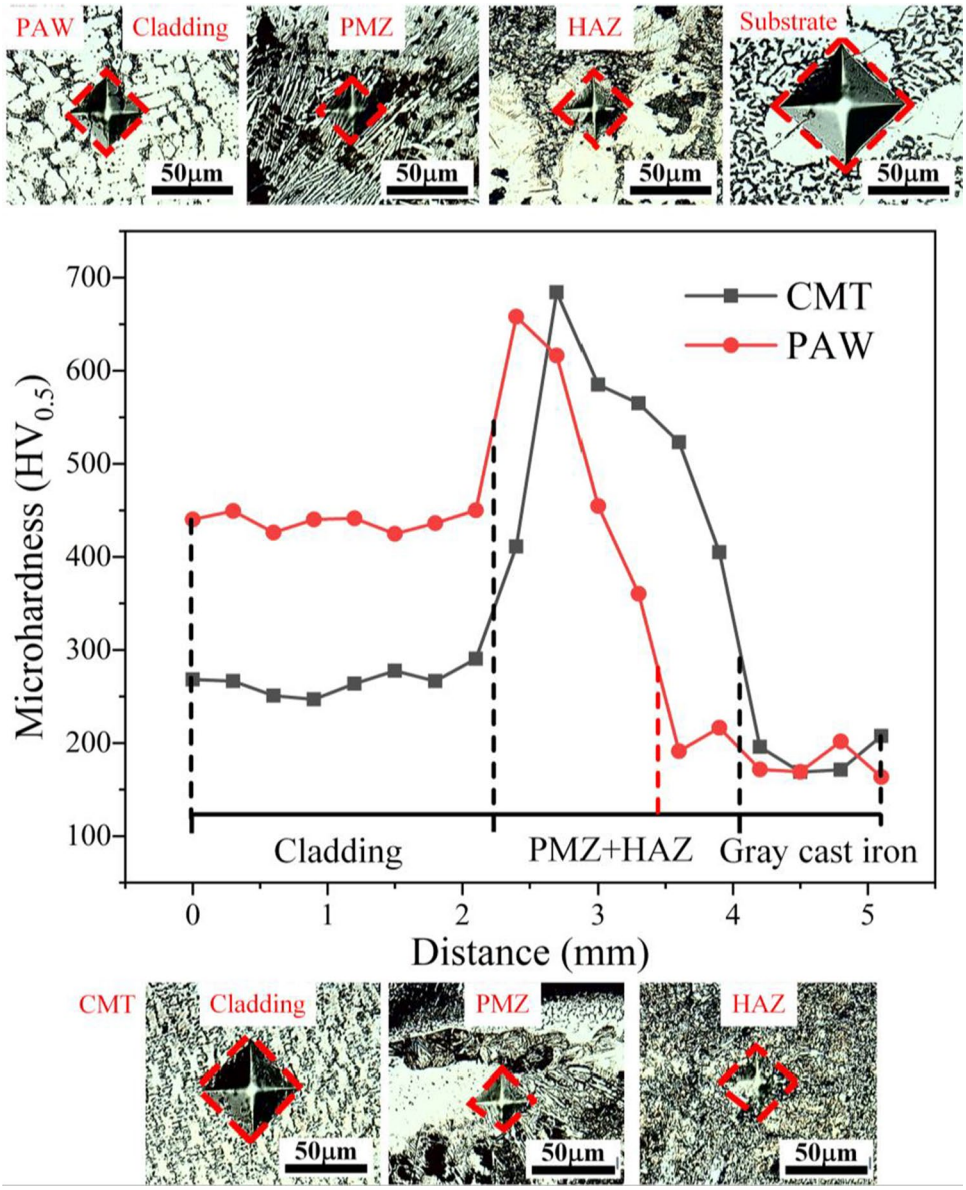

Fig. 16 Microhardness distribution of CMT and PAW deposited specimens

2. Microstructure of CMT deposited layer is mainly γ-Ni solid solution with (Nb, Mo) carbides along the grain boundary, and microstructure of PAW deposited layer is (Fe, Ni) solid solution with eutectic of (Fe, Ni, Cr) solid solution and carbides.
3. A significant transition zone for CMT deposits was produced near interface, and its microstructure is mainly composed of martensite, ledeburite, and unfused graphite. Microstructure of both HAZ is mainly martensite, pearlite, and lamellar graphite. Cracks appeared in HAZ and PMZ of CMT due to formation of high carbon twin martensite.
4. Microhardness of PAW deposited layer is greater than that of CMT, and the highest hardness appears in the PMZ. The shear fracture at the interface of the deposited layers presents intergranular fracture.

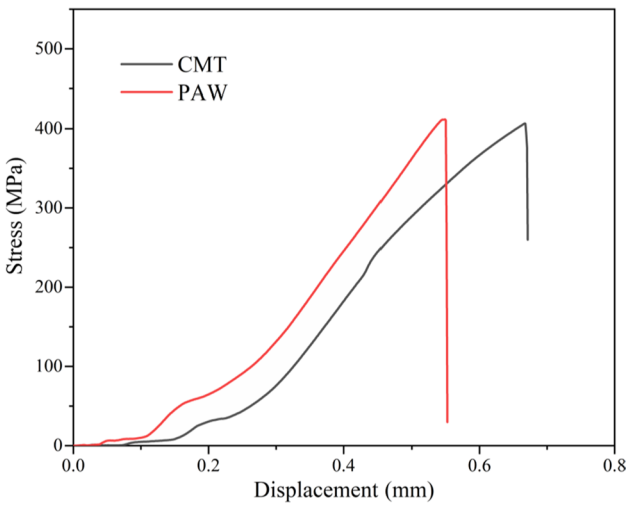

Fig. 17 Displacement-stress curves of deposited samples

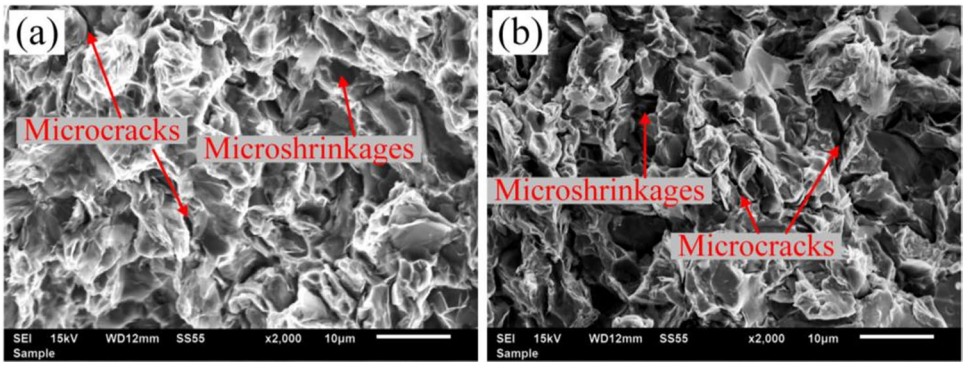

Fig. 18 Fracture morphology of CMT and PAW sheared specimens, **a** CMT, 955 J/mm, **b** PAW, 1374 J/mm

Funding This work was supported by the National Natural Science Foundation of China No. 52005007 and No. 52105312.

Declarations

Conflict of interest The authors declare no competing interests.

References

1. Cueva G, Sinatora A, Guesser WL, Tschiptschin AP (2003) Wear resistance of cast irons used in brake disc rotors. Wear 255:1256–1260
2. Yang P, Song Y, Wang J, Hu FY, Xie LW (2021) Semiconductor laser cladding of an Fe-based alloy on nodular cast iron. Weld World 65:785–792
3. Keller J, Fridrici V, Kapsa P, Vidaller S, Huard JF (2007) Influence of chemical composition and microstructure of gray cast iron on wear of heavy duty diesel engines cylinder liners. Wear 263:1158–1164
4. Mitelea I, Bordeaşu I, Riemschneider E, Drˇagos Utu I, Craciunescu CM (2022) Cavitation erosion improvement following TIG surface-remelting of gray cast iron. Wear 496:204282
5. Zhu LJ, Liu YH, Li ZW, Zhou L, Li YJ, Xiong AH (2020) Microstructure and properties of Cu-Ti-Ni composite coatings on gray cast iron fabricated by laser cladding. Opt Laser Technol 122:105879
6. Zhong ML, Liu WJ, Zhang HJ (2006) Corrosion and wear resistance characteristics of NiCr coating by laser alloying with powder feeding on grey iron liner. Wear 260:1349–1355
7. Manikandan SGK, Sivakumar D, Rao KP, Kamaraj M (2016) Effect of enhanced cooling on microstructure evolution of alloy 718 using the gas tungsten arc welding process. Weld World 60:1–16
8. Wang JF, Sun QJ, Wang H, Liu JP, Feng JC (2016) Effect of location on microstructure and mechanical properties of additive layer manufactured Inconel 625 using gas tungsten arc welding. Mater Sci Eng A 676:395–405
9. Abioye TE, Folkes J, Clare AT (2013) A parametric study of Inconel 625 wire laser deposition. J Mater Process Technol 213:2145–2151
10. Abioye TE, Farayibi PK, Clare AT (2017) A comparative study of Inconel 625 laser cladding by wire and powder feedstock. Mater Manuf Process 32:1653–1659
11. Prabu SS, Ramkumar KD, Arivazhagan N (2017) Effect of filler metals on the mechanical properties of Inconel 625 and AISI 904L dissimilar weldments using gas tungsten arc welding. Mater Sci Eng 263:062072
12. Frei J, Alexandrov BT, Rethmeier M (2016) Low heat input gas metal arc welding for dissimilar metal weld overlays part I: the heat-affected zone. Weld World 60:459–473
13. Huang JK, Liu SE, Yu SR, An L, Yu XQ, Fan D, Yang FQ (2020) Cladding Inconel 625 on cast iron via bypass coupling micro-plasma arc welding. J Manuf Process 56:106–115
14. Arias-González F, Del Val J, Comesaña R, Penide J, Lusquinos F, Quintero F, Riveiro A, Boutinguiza M, Pou J (2016) Fiber laser cladding of nickel-based alloy on cast iron. Appl Surf Sci 374:197–205
15. Fesharaki MN, Shoja-Razavi R, Mansouri HA, Jamali H (2019) Evaluation of the hot corrosion behavior of Inconel 625 coatings on the Inconel 738 substrate by laser and TIG cladding techniques. Opt Laser Technol 111:744–53
16. Sadeghi A, Moloodi A, Golestanipour M, Shahri MM (2017) An investigation of abrasive wear and corrosion behavior of surface repair of gray cast iron by SMAW. J Mater Res Technol 6:90–95
17. Abboud JH (2012) Microstructure and erosion characteristic of nodular cast iron surface modified by tungsten inert gas. Mater Des 35:677–684
18. Shi KY, Hu SB, Zheng HF (2011) Microstructure and fatigue properties of plasma transferred arc alloying TiC-W-Cr on gray cast iron. Surf Coat Technol 206:1211–1217
19. Ghaini FM, Ebrahimnia M, Gholizade S (2011) Characteristics of cracks in heat affected zone of ductile cast iron in powder welding process. Eng Fail Anal 18:47–51
20. Collini L, Nicoletto G, Konecn'a R (2008) Microstructure and mechanical properties of pearlitic gray cast iron. Mater Sci Eng A 488:529–539
21. Pickin CG, Williams SW, Lunt M (2011) Characterisation of the cold metal transfer (CMT) process and its application for low dilution cladding. J Mater Process Technol 211:496–502
22. Xu LY, Shao CS, Tian L, Zhang JL, Han YD, Zhao L, Jing HY (2022) Intergranular corrosion behavior of Inconel 625 deposited by CMT/GTAW. Corros Sci 201:110295
23. Ruiz-Vela JI, Montes-Rodríguez JJ, Rodríguez-Morales E, Toscano-Giles JA (2019) Effect of cold metal transfer and gas tungsten arc welding processes on the metallurgical and mechanical properties of Inconel® 625 weldings. Weld World 63:459–479
24. Sahoo A, Tripathy S (2021) Development in plasma arc welding process: a review. Mater Today: Proc 41:363–368
25. Chen SJ, Zhang RY, Jiang F, Goecke S (2018) A novel method for testing the electrical property of arc column in plasma arc welding. Weld World 62:637–645
26. He K, Dong LJ, Wang QY, Zhang HL, Li YF, Liu L, Zhang Z (2022) Comparison on the microstructure and corrosion behavior of Inconel 625 cladding deposited by tungsten inert gas and cold metal transfer process. Surf Coat Technol 435:128245
27. Varghese P, Vetrivendan E, Dash MK, Ningshen S, Kamaraj M, Mudali UK (2019) Weld overlay coating of Inconel 617M on type

316L stainless steel by cold metal transfer process. Surf Coat Technol 357:1004–1013
28. Feng K, Chen Y, Deng PS, Li YY, Li ZG (2017) Improved high-temperature hardness and wear resistance of Inconel 625 coatings fabricated by laser cladding. J Mater Process Technol 243:82–91
29. Wang YH, Konovalov S, Chen XZ, Singh RA, Jayalakshmi S (2022) Research on plasma arc additive manufacturing of Inconel 625 Ni–Cu functionally graded materials. Mater Sci Eng A 853:143796
30. Shen QK, Xue JX, Yu XY, Zheng ZH, Ou N (2022) Triple-wire plasma arc cladding of Cr-Fe-Ni-Tix high-entropy alloy coatings. Surf Coat Technol 443:128638
31. Xie FW, He YH, Yuan ZR, Kang XY (2022) Microstructure and high-temperature sliding wear performance of Fe-Co-Mo alloy coating fabricated by plasma cladding. Surf Coat Technol 444:128667
32. Mazenc A, Galtayries A, Seyeux A, Marcusa P, Leclercq S (2013) ToF-SIMS study of the behavior of thermally oxidized films formed on nickel-based 690 alloy in high-temperature water. Surf Interface Anal 45:583–586
33. Alvaraes CP, Jorge JCF, de Souza LFG, Arau'jo LS, Mendes MC, Farneze HN (2020) Microstructure and corrosion properties of single layer Inconel 625 weld cladding obtained by the electroslag welding process. J Mater Res Technol 9:16146–16158
34. Mookara RK, Seman S, Jayaganthan R, Amirthalingam M (2021) Influence of droplet transfer behaviour on the microstructure, mechanical properties and corrosion resistance of wire arc additively manufactured Inconel (IN) 625 components. Weld World 65:573–588
35. Yu J, Song B, Liu YC (2018) Microstructure and wear behaviour of Ni-based alloy coated onto grey cast iron using a multi-step induction cladding process. Results Phys 10:339–345
36. Jeshvaghani RA, Jaberzadeh M, Zohdi H, Shamanian M (2014) Microstructural study and wear behavior of ductile iron surface alloyed by Inconel 617. Mater Des 54:491–497
37. Liu L, Feng C, Li R (2020) Applications of nickel-based alloy for oil country tubular goods. Mater Sci Forum 993:604–609
38. Xu X, Mi GY, Chen L, Xiong LD, Jiang P, Shao XY, Wang CM (2017) Research on microstructures and properties of Inconel 625 coatings obtained by laser cladding with wire. J Alloy Compd 715:362–373
39. Ebrahimnia M, Ghaini FM, Gholizade S, Salari M (2012) Effect of cooling rate and powder characteristics on the soundness of heat affected zone in powder welding of ductile cast iron. Mater Des 33:551–556
40. Meng W, Lei YL, Wang X, Ma QS, Hu L, Xie H, Yin XH (2022) Interface characteristics and mechanical properties of wire-arc depositing Inconel 625 superalloy on ductile cast iron. Surf Coat Technol 440:128493
41. Ma QS, Chen HZ, Ren NN, Zhang YY, Hu L, Meng W, Yin XH (2021) Effects of ultrasonic vibration on microstructure, mechanical properties, and fracture mode of Inconel 625 parts fabricated by cold metal transfer arc additive manufacturing. J Mater Eng Perform 30:6808–6820
42. Solecka M, Petrzak P, Radziszewska A (2015) The microstructure of weld overlay Ni-base alloy deposited on carbon steel by CMT method. Trans Tech Publ Ltd 231:119–124
43. Ghaini FM, Ebrahimnia M, Gholizade S (2011) Characteristics of cracks in heat affected zone of ductile cast iron in powder welding process. Eng Fail Anal 18:47–51
44. Liu YC, Zhan XH, Yi P, Liu T, Liu BL, Wu Q (2018) Research on the transformation mechanism of graphite phase and microstructure in the heated region of gray cast iron by laser cladding. Opt Laser Technol 100:79–86
45. Fan KL, He GQ, She M, Liu XS, Lu Q, Yang Y, Tian DD, Shen Y (2014) High-temperature low cycle fatigue behavior of a gray cast iron. Mater Charact 98:37–46

Publisher's note Springer Nature remains neutral with regard to jurisdictional claims in published maps and institutional affiliations.

Springer Nature or its licensor (e.g. a society or other partner) holds exclusive rights to this article under a publishing agreement with the author(s) or other rightsholder(s); author self-archiving of the accepted manuscript version of this article is solely governed by the terms of such publishing agreement and applicable law.